RESEARCH ARTICLE | NOVEMBER 13 2025

Electromagnetic field solver for QED polarization in super-strong magnetic fields of magnetars and laser plasmas

M. Alawashra ; J. Benáček ; M. Pohl ; M. V. Medvedev

Phys. Plasmas 32, 113903 (2025)
https://doi.org/10.1063/5.0286700
CHORUS

Electromagnetic field solver for QED polarization in super-strong magnetic fields of magnetars and laser plasmas

Cite as: Phys. Plasmas **32**, 113903 (2025); doi: 10.1063/5.0286700
Submitted: 20 June 2025 · Accepted: 7 October 2025 ·
Published Online: 13 November 2025

View Online Export Citation CrossMark

M. Alawashra,[1,a)] J. Benáček,[2,a)] M. Pohl,[1,2] and M. V. Medvedev[3,4]

AFFILIATIONS

[1]Deutsches Elektronen-Synchrotron DESY, Platanenallee 6, 15738 Zeuthen, Germany
[2]Institute for Physics and Astronomy, University of Potsdam, Karl-Liebknech-Str. 24/25, 14476 Potsdam, Germany
[3]Department of Physics and Astronomy, University of Kansas, Lawrence, Kansas 66045, USA
[4]Laboratory for Nuclear Science, Massachusetts Institute of Technology, Cambridge, Massachusetts 02139, USA

[a)]**Authors to whom correspondence should be addressed:** mahmoud.al-awashra@desy.de and jan.benacek@uni-potsdam.de

ABSTRACT

Superstrongly magnetized plasmas play a crucial role in extreme environments of magnetars and laboratory laser experiments, demanding a comprehensive understanding of how quantum electrodynamic (QED) effects influence plasma behavior. Earlier analytical and semi-analytical calculations have shown that QED effects can significantly modify the plasma polarization mode behavior around magnetars. In this work, we present the first electromagnetic field solver that is valid in the range from $B \to 0$ to beyond the Schwinger limit. QED vacuum polarization in superstrong magnetic fields is modeled with nonlinear Maxwell equations. We show that electromagnetic waves in simulations follow the analytical solutions well and reproduce the birefringence effects of electromagnetic wave modes between the O and X polarizations of perpendicular electromagnetic waves and those between L and R polarizations of parallel waves. This new framework can be applied to kinetic as well as other types of computer simulations. The solver's key advantage lies in its versatility, allowing it to be used in gyro-motion, gyro-center, and gyro-kinetic simulations, which do not resolve the cyclotron motion, or in plasma studies with ground-level Landau quantization.

I. INTRODUCTION

The magnetic field strength in magnetar magnetospheres, as well as in laboratory laser plasma experiments, can exceed the Schwinger quantum limit of $B_Q \approx 4.4 \times 10^{13}$ G constraining the validity of classical theories of electromagnetism. In such superstrong magnetic fields, the vacuum behaves as a polarized medium because of the interaction of the electromagnetic fields with virtual electron–positron pairs. As a result, a photon traveling through this magnetized environment can undergo refraction or wave-splitting phenomena that are not allowed in classical electrodynamics.

The magnetars, often considered the "central engines" of gamma-ray bursts, x-ray flares, and fast radio bursts, have magnetic fields whose strength reaches 10^{15}–10^{17} G (Mereghetti *et al.*, 2005; Rowlinson *et al.*, 2014; and Younes *et al.*, 2023). Some pulsars, such as PSR J1846-0258 and PSR J1119-6127, can also reach this limit under the assumption that the magnetic field strength determines the stellar spin down by the dipole radiation (Gotthelf *et al.*, 2000). For multipolar radiation, the magnetic fields of pulsars or magnetars are also predicted to exceed the quantum limit (Gil and Mitra, 2001). Therefore, highly magnetized neutron stars serve as natural laboratories for testing quantum electrodynamics (QED) in the strong-field regime, offering a unique opportunity to study its effects and implications.

Observations of magnetar x-ray polarization can provide a crucial test of the QED effects in superstrong magnetic fields. A key effect, vacuum birefringence, reflecting a modified vacuum dielectricity and permeability, can explain the x-ray polarization observed from magnetars like 4U 0142 + 61 (Taverna *et al.*, 2022; Rigoselli *et al.*, 2025; and Taverna and Turolla, 2024). The birefringence could provide photons at higher energies and those at lower energies with orthogonal polarization (Taverna *et al.*, 2015).

In the quantum regime of vacuum polarization, QED effects cause polarization-dependent refraction by modifying the wave speeds of the ordinary (O) and extraordinary (X) modes (Schwinger, 1951; Thompson and Kostenko, 2020; and Pérez-García *et al.*, 2023). In the *O* mode, the electric field oscillates in the plane of the propagation vector **k** and the magnetic field **B**, while in the *X* mode, it oscillates perpendicular to both. However, right- (R) and left- (L) circularly polarized modes, propagating parallel to **B**, remain unaffected, preserving their classical behavior. There are also several other effects on particle interaction in the quantum regime (Kostenko and Thompson, 2018, 2019).

Previous studies on vacuum birefringence and quantum refraction in strong magnetic fields have relied on one-loop QED effective-action approaches (Caiazzo and Heyl, 2018, 2020; Caiazzo, 2019; and Caiazzo *et al.*, 2022). Such a formalism was used to study the vacuum birefringence and quantum refraction in pulsar magnetospheres, applying it to the Goldreich–Julian (GJ) model (Kim and Kim, 2023) and to a practical model of pulsar emission (Kim *et al.*, 2024). Though insightful, these methods assume uniform fields and neglect nonlinear plasma dynamics. In contrast, kinetic simulations such as particle-in-cell (PIC) simulations can provide a better picture by self-consistently solving nonlinear Maxwell's equations, including QED effects, capturing the nonlinear interactions and plasma feedback that are essential for describing realistic astrophysical and laboratory environments.

Recent and next-generation laser facilities, such as Ultrashort pulse laser System (ZEUS), Center for relativistic Laser Science (CORELS), and Laser Und XFEL Experiment (LUXE) (Bromage *et al.*, 2019; Danson *et al.*, 2019; and Borysova and On Behalf of LUXE, 2021), approach the quantum limit (Zhang *et al.*, 2020; Gonoskov *et al.*, 2022), in laser physics often denoted as the "critical limit." The QED polarization correction for the intensity of electromagnetic fields below the Schwinger limit has been developed (Blinne *et al.*, 2019; Grismayer *et al.*, 2021; and Lindner *et al.*, 2023), and pair-producing mechanisms have been added for laser plasma simulations (Grismayer *et al.*, 2016; Schoeffler *et al.*, 2019, 2023; Qu *et al.*, 2022; and Zhang *et al.*, 2025). The nonlinear Maxwell equations for the case of the weak fields ($E \ll E_Q$ and $B \ll B_Q$) were implemented in (Zhang *et al.*, 2025), following the spatial and temporal evolution of the electromagnetic field in multi-dimensional simulations, which can be suitable for the PIC loop. However, the numerical implementation for strong magnetic fields, $B \gg B_Q$, remains open.

The weak-field approximation is valid only below the quantum field limit, and therefore one needs to consider Maxwell's equations for superstrong magnetic fields to study plasma environments in the quantum regime. A general analytical form of the modified Maxwell's equation can be derived if the electric field vanishes and the magnetic field is strong, $E \ll E_Q$, $B \gtrsim B_Q$ (Heisenberg and Euler, 2006; Lundin, 2010).

In this work, we introduce the first numerical algorithm for solving the spatial and temporal evolution of the electromagnetic field in the quantum regime. We develop a numeric electromagnetic-field solver that can be used in electromagnetic and kinetic plasma simulations of magnetar magnetospheres and laser plasmas. Specifically, we aim to implement, employ, and test the field solver in the PIC simulation method.

The paper is structured as follows. In Sec. II, we introduce the QED polarization nonlinear effects in Maxwell's equations. The new numerical scheme for the field solver is developed, and the PIC simulation setup is described in Sec. III. The results of the numerical tests and stability are presented in Sec. IV. We discuss the strengths and limits of the proposed scheme in Sec. V and state conclusions in Sec. VI.

II. NONLINEAR MAXWELL'S EQUATIONS

In classical electrodynamics, the vacuum is considered an empty passive space in which particles and fields move and interact. Maxwell's equations, which describe these interactions, are linear in nature and are driven by charges and currents. However, when electromagnetic fields reach high intensities, quantum electrodynamics (QED) effects become significant, introducing nonlinearities into Maxwell's equations. These nonlinearities are result of the polarization of the quantum vacuum.

The quantum vacuum fluctuations of virtual electron–positron pairs can mediate the exchange of energy and momentum between photons. In the effective field theory framework, the Heisenberg–Euler Lagrangian density, $\mathscr{L}_{\rm HE}$, encapsulates all orders of the one-loop photon–photon interaction processes. This Lagrangian is added as the leading correction to the standard Maxwell Lagrangian density, $\mathscr{L}_{\rm M}$, with the one-loop corrections Lagrangian density being $\mathscr{L} = \mathscr{L}_{\rm M} + \mathscr{L}_{\rm HE}$ where

$$\mathscr{L}_{\rm M} = -\frac{1}{16\pi} F_{\mu\nu} F^{\mu\nu} - \frac{1}{c} A_\mu j^\mu, \tag{1}$$

and (Heisenberg and Euler, 2006; Medvedev, 2023)

$$\mathscr{L}_{\rm HE} = \frac{m_e c^2}{8\pi^2} \left(\frac{m_e c}{\hbar}\right)^3 \int_0^\infty \frac{e^{-\eta}}{\eta^3} \left[-(\eta a \cot \eta a)(\eta b \coth \eta b) + 1 - \frac{\eta^2}{3}(a^2 - b^2) \right] d\eta. \tag{2}$$

Here, $F_{\mu\nu} = \partial_\mu A_\nu - \partial_\nu A_\mu$ is the electromagnetic field tensor, A_ν is the four-potential, j^μ is the four-current density, and the scalar parameters a and b are given by the covariant form

$$a = -\frac{i\hbar e}{\sqrt{2} m_e^2 c^3} \left[(\mathscr{F} + i\mathscr{G})^{1/2} - (\mathscr{F} - i\mathscr{G})^{1/2} \right], \tag{3}$$

$$b = \frac{\hbar e}{\sqrt{2} m_e^2 c^3} \left[(\mathscr{F} + i\mathscr{G})^{1/2} + (\mathscr{F} - i\mathscr{G})^{1/2} \right], \tag{4}$$

and therefore, they are valid in all reference frames. Here, the invariant scalar quantities, $\mathscr{F}$ and $\mathscr{G}$ are given by

$$\mathscr{F} = \frac{1}{4} F_{\mu\nu} F^{\mu\nu} = \frac{1}{2} (\mathbf{B}^2 - \mathbf{E}^2), \tag{5}$$

and

$$\mathscr{G} = \frac{1}{4} \hat{F}_{\mu\nu} \hat{F}^{\mu\nu} = -\mathbf{B} \cdot \mathbf{E}, \tag{6}$$

where the Hodge dual tensor is given by $\hat{F}^{\mu\nu} = \frac{1}{2} \varepsilon^{\mu\nu\gamma\delta} F_{\gamma\delta}$, where $\varepsilon^{\mu\nu\gamma\delta}$ is the Levi–Civita symbol. The parameters a and b can be rewritten in the following form:

$$a = \frac{E}{E_Q}, \quad b = \frac{B}{B_Q}, \tag{7}$$

where E_Q and B_Q are the quantum electric and magnetic field strengths.

Though the general analytical form of the QED modified Maxwell equations is unknown, one can obtain an analytical form under different conditions. Modified Maxwell's equations can be obtained analytically in the case of electromagnetic fields smaller than the quantum field limit ($E \ll E_Q$ and $B \ll B_Q$). The nonlinear Maxwell's equations for the case of the weak fields were implemented in Grismayer *et al.* (2021). Here, we consider Maxwell's equations in a superstrong magnetic field by following the general analytical form of the modified Maxwell's equations for a vanishing electric field, $E \ll E_Q$, and an arbitrarily strong magnetic field, from $B \to 0$ to $B \gg B_Q$ (Heisenberg and Euler, 2006; Lundin, 2010).

The electromagnetic field equations are obtained from the variational principle for action. By performing a variation of the fields and requiring the variation to vanish, $\delta S = \delta \int \mathrm{d}^4 x \mathscr{L}$, we get the Euler–Lagrange equations

$$\partial_\mu \frac{\partial \mathscr{L}}{\partial F_{\mu\nu}} = \frac{1}{2c} j^\nu, \tag{8}$$

substituting the full Lagrangian density including the Heisenberg–Euler Lagrangian density, Eq. (2), the nonlinear Maxwell's equations take the form Lundin (2010)

$$\gamma_{\mathscr{F}} \partial_\mu F^{\mu\nu} + \frac{1}{2}\left[\gamma_{\mathscr{F}\mathscr{F}} F^{\mu\nu} F_{\alpha\beta} + \gamma_{\mathscr{G}\mathscr{G}} \hat{F}^{\mu\nu} \hat{F}_{\alpha\beta} + \gamma_{\mathscr{F}\mathscr{G}} \left(F^{\mu\nu} \hat{F}_{\alpha\beta} + \hat{F}^{\mu\nu} F_{\alpha\beta}\right)\right] \partial_\mu F^{\alpha\beta} = \frac{1}{c} j^\nu, \tag{9}$$

where QED coupling scalars are given as $\gamma_{\mathscr{F}} = \partial \mathscr{L}/\partial \mathscr{F}$, $\gamma_{\mathscr{F}\mathscr{G}} = \partial^2 \mathscr{L}/\partial \mathscr{F} \partial \mathscr{G}$, etc. For the case of vanishing electric fields, $\mathbf{E} \to 0$, and non-zero magnetic fields, $\mathbf{B} \neq 0$, the QED coupling scalars can be calculated analytically to be the following Lundin (2010) and Medvedev (2023)

$$\gamma_{\mathscr{F}} = \frac{-1 + C_\delta(b)}{4\pi}, \tag{10}$$

$$\gamma_{\mathscr{F}\mathscr{F}} = \frac{C_\mu(b)}{4\pi B^2}, \tag{11}$$

$$\gamma_{\mathscr{G}\mathscr{G}} = \frac{C_\varepsilon(b)}{4\pi B^2}, \tag{12}$$

$$\gamma_{\mathscr{F}\mathscr{G}} = 0, \tag{13}$$

where the parameters C_δ, C_μ, and C_ε are all dependent on the normalized magnetic field, $b = B/B_Q$, and given analytically by Eqs. (28)–(30) in Medvedev (2023). We plot in Fig. 1 those parameters as a function normalized magnetic field. Note that all the parameters approach zero as the magnetic field becomes $B \ll B_Q$, recovering the classical Maxwell equations in Eq. (9) in this regime.

Expressing Eq. (9) explicitly in terms of the electric, **E**, and magnetic, **B**, fields gives the modified Gauss' law

$$\gamma_{\mathscr{F}}\ \nabla \cdot \mathbf{E} + \gamma_{\mathscr{F}\mathscr{F}}\ \mathbf{E} \cdot \nabla\left(\frac{\mathbf{B}^2 - \mathbf{E}^2}{2}\right) + \gamma_{\mathscr{G}\mathscr{G}}\ \mathbf{B} \cdot \nabla(-\mathbf{B} \cdot \mathbf{E}) = -\rho, \tag{14}$$

and the modified Ampère's law

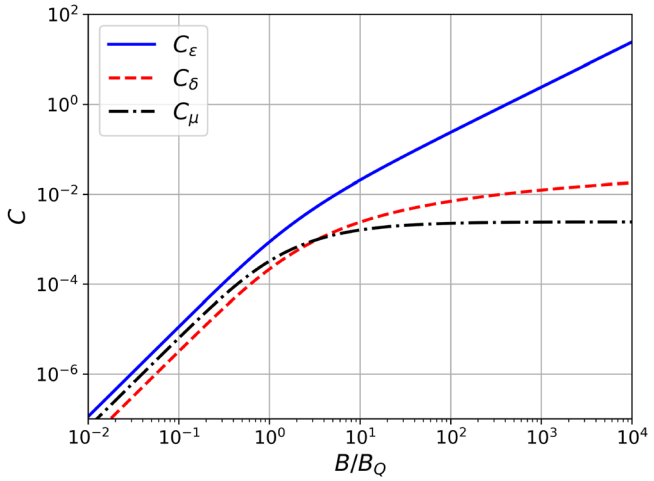

FIG. 1. QED parameter C_ε, C_δ, and C_μ as functions of the normalized magnetic field B/B_Q. All the parameters approach zero as the magnetic field becomes $B \ll B_Q$, recovering the classical Maxwell equations in this regime.

$$\gamma_{\mathscr{F}}\left[\frac{1}{c}\frac{\partial}{\partial t}\mathbf{E} - \nabla \times \mathbf{B}\right] + \gamma_{\mathscr{F}\mathscr{F}}\left[\mathbf{E}\frac{1}{c}\frac{\partial}{\partial t}\left(\frac{\mathbf{B}^2 - \mathbf{E}^2}{2}\right) + \mathbf{B} \times \nabla\left(\frac{\mathbf{B}^2 - \mathbf{E}^2}{2}\right)\right] + \gamma_{\mathscr{G}\mathscr{G}}\left[\mathbf{B}\frac{1}{c}\frac{\partial}{\partial t}(-\mathbf{B} \cdot \mathbf{E}) - \mathbf{E} \times \nabla(-\mathbf{B} \cdot \mathbf{E})\right] = \frac{1}{c}\mathbf{j}. \tag{15}$$

As for the other pair of Maxwell's equations, $\partial_\nu \hat{F}^{\mu\nu} = 0$, we retain the same equations as the classical case

$$\nabla \cdot \mathbf{B} = 0, \tag{16}$$

and

$$\frac{1}{c}\frac{\partial \mathbf{B}}{\partial t} + \nabla \times \mathbf{E} = 0. \tag{17}$$

Therefore, including the QED corrections in PIC simulation, we expect a modification of the electric field advance (Ampère's law) and no modification of the magnetic field 1.

III. NUMERICAL METHODS

In this section, we introduce the main features of the new PIC field solver, including the QED polarization effects. The standard PIC method uses a set of macroparticles with fixed shapes to represent the distribution function. This approach allows the distribution function to be updated by tracking the movement of the computational particles, while the Maxwell equations are solved on a discretized spatial grid. First, we introduce a novel field solver in Sec. III A that solves the nonlinear Maxwell equations in the presence of superstrong magnetic fields. Then, we present the implementation of this solver in the PIC algorithm in Sec. III B. Numerical effects arising from space and time discretization are briefly discussed in Sec. III C. Finally, in Sec. III D, we present the simulation setup we used to test the new field solver. More details are given in Appendixes A, B, and C.

A. Electromagnetic solver in superstrong magnetic fields approach

The widely used second-order finite-difference time-domain (FDTD) method for solving Maxwell's equations on a spatial grid is

the Yee scheme (Yee, 1966). This scheme simultaneously computes the magnetic and electric fields by discretizing and solving Faraday's and Ampère's laws, respectively. The Yee scheme uses a leapfrog approach, where fields are shifted in space and time, thus ensuring robustness and second-order accuracy while eliminating the need to solve coupled equations or perform matrix inversions. This leapfrog approach is only possible due to the explicit linear relationship between the fields in Maxwell's equations. Furthermore, the algorithm's simplicity and computational efficiency make it well-suited for implementation in parallelized numerical codes, facilitating the performance of large-scale simulations.

We developed a modified Yee electric field solver on the Yee lattice that uses the QED-modified Ampère law in the strong-field limit [Eq. (15)]. In Eq. (15), the temporal derivatives of the different electric field components are mixed in each spatial component of the equation, unlike the linear relation in Ampère law. Therefore, the temporal derivatives of each electric field component are calculated separately in three-dimensional space. In a one-dimensional approach, the E_y and E_z components are known in the same spatial position, allowing their calculation at once.

We have outlined a series of analytical procedures to achieve this in Appendix A, finding the following expression for the temporal derivative of the electric field:

$$\frac{\partial \mathbf{E}}{\partial t} = A^{-1}\left(\frac{1}{c}\mathbf{j} - \mathbf{Q}\right), \tag{18}$$

where A^{-1} is the inverse matrix of an 3×3 matrix A given by

$$A_{ij} = \frac{1}{c}\left[\gamma_{\mathscr{F}}\delta_{ij} - \gamma_{\mathscr{F}\mathscr{F}}E_iE_j - \gamma_{\mathscr{G}\mathscr{G}}B_iB_j\right], \tag{19}$$

with the indices i and j both looping over the spatial dimensions x, y, and z, $\mathbf{j}$ is the electric current vector and $\mathbf{Q}$ is a vector with dependence on the spatial derivatives of the electric and magnetic fields and the magnetic field temporal derivative. The components of the vector, $\mathbf{Q}$, are given by Eqs. (A3)–(A5). For an accurate estimate of the magnetic field time derivative in $\mathbf{Q}$ [also seen in Eq. (15)], we substitute its value from Faraday's law [Eq. (17)], yielding at the end the vector $\mathbf{Q}$ to be dependent only on the spatial derivatives of the electromagnetic fields. Note that Eqs. (18) and (19) recover the classical Maxwell equations in the $B \ll B_Q$ regime, where the matrix A becomes unitary and the factor Q recovers the $\mathbf{V} \times \mathbf{B}$ term. This makes the solver valid for both regimes. The numerical implementation of this field solver [Eq. (18)] is explained in Appendix C, and the numerical code is available at the Zenodo platform (DOI: https://doi.org/10.5281/zenodo.15004304).

B. Updated particle-in-cell method

We have updated the PIC algorithm by the nonlinearity of the modified Ampère Eq. (18), which requires additional steps in the leapfrog algorithm. Here, we summarize those modifications, with the detailed modifications given in Appendix C.

Note that the nonlinear Ampère law given in Eq. (18) couples all the field components of $\mathbf{E}$ and $\mathbf{B}$. Therefore, the numerical solution of Eq. (18) requires the evaluation of the fields at all the grid points where the electric field is shifted on the Yee lattice. To do this, we linearly interpolate the fields using the nearest grid points.

We also note that solving Eq. (18) with the centered-difference time partial derivative requires knowledge of $\mathbf{E}$ at the half-time step. To preserve the same order of the time derivative of the Yee scheme, we first predict the electric fields at the half-time step using the QED modified solver in forward time derivatives, and then, we use the fields at the half-time step to evolve the electric field to the full time step using a centered time derivative. The comparison of the original and the new method is shown in Fig. 2.

C. Numerical stability

The Yee algorithm can produce nonphysical effects such as numerical wave dispersion when applied to nonlinear or linear Maxwell's equations. This is due to the finite differencing of spatial and temporal derivatives of the Yee scheme. For example, the phase velocity of numerical wave modes may deviate from the speed of light c, depending on the wavelength and propagation direction. This discrepancy results in phase errors or delays of the propagating waves, leading to artifacts. Therefore, understanding the numerical dispersion is essential for assessing the Yee algorithm's behavior and accuracy limits, particularly for the cases when the superstrong magnetic fields change linear Maxwell's equations significantly.

We employ the standard mode analysis approach to analyze the numerical stability of the new QED polarization solver (Greenwood *et al.*, 2004). In the case of linear Maxwell's equation, the plasma dispersion relation for a plane electromagnetic wave propagating in a one-dimensional Yee grid is

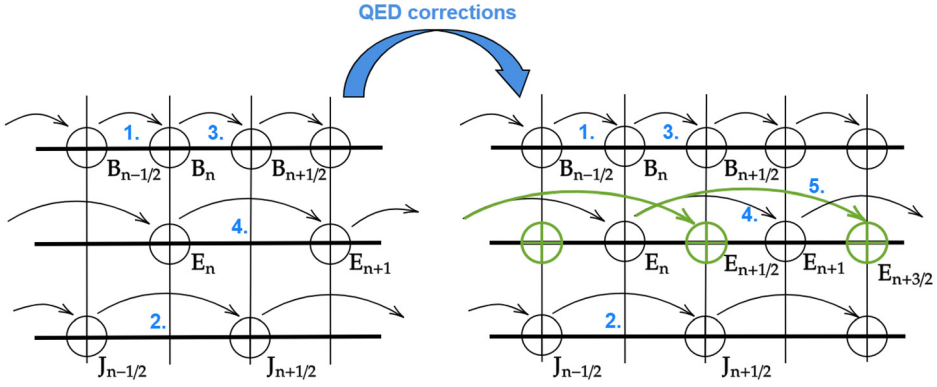

FIG. 2. The original (left) and QED polarization updated (right) PIC scheme for the advancement of plasma quantities. In the new scheme, step 4 is still time-centered at time step $n+\frac{1}{2}$ and uses the predictor result at $n+\frac{1}{2}$. Step 5 is a predictor going from n to $n+\frac{3}{2}$ but still time-centered at $n+\frac{1}{2}$. Both steps 4 and 5 employ the use of the new solver.

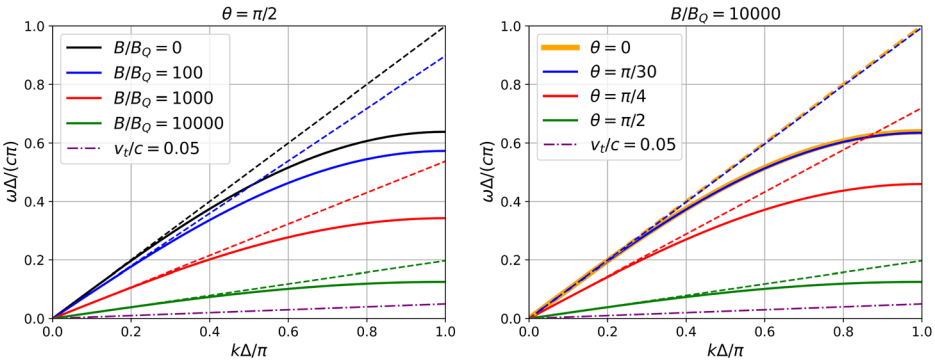

FIG. 3. Dispersion relation of the O-mode waves, including the QED modification, given by Eq. (21). Solid lines are the numerical dispersion curves; dashed lines are the analytically derived dispersion curves. The left figure includes the waves propagating perpendicular, $\theta = \pi/2$, to the homogeneous magnetic field with different strengths, B/B_Q. The right figure includes the waves propagating with different obliquity angles to the homogeneous magnetic fields with a strength $B/B_Q = 10000$. The purple dashed-dotted curve shows the slope of the thermal velocity of the particles in the test PIC simulation in Sec. III D. The curves with $B/B_Q = 0$ and $\theta = 0$ are identical. The FDTD parameters are $\Delta_x = \Delta$ and $\Delta t = 0.4\Delta/c$.

$$\left(\frac{c\Delta t}{\Delta x}\right)^2 \sin^2\left(\frac{k\Delta x}{2}\right) - \sin^2\left(\frac{\omega\Delta t}{2}\right) = 0, \tag{20}$$

where Δx and Δt are the spatial and time steps, respectively, and ω and k are the wave frequency and wave number, respectively. Notice that for the case, $\Delta t = \Delta x/c$, the numerical dispersion relation recovers the physical electromagnetic dispersion relation, $\omega = kc$.

In Appendix B, we derive the numerical dispersion relation for the nonlinear Maxwell's equations in the superstrong magnetic field case. We introduce here the final result of the dispersion relations, and one can refer to the detailed calculations in Appendix B.

We consider a plane wave propagating in the x direction and derive the dispersion relations for a homogeneous magnetic field in the $x-y$ plane, $\mathbf{B_0} = \mathrm{B}_0 \cos\theta\hat{x} + \mathrm{B}_0 \sin\theta\hat{y}$. For the extraordinary electromagnetic mode (X mode) and $\theta \neq 0$, where the wave-like perturbation components are δB_y, δE_x, and δE_z, we found the following dispersion relation [Eq. (B7)]:

$$\left(\frac{1 - C_\delta - C_\mu \sin^2\theta}{1 - C_\delta}\right)\left(\frac{c\Delta t}{\Delta x}\right)^2 \sin^2\left(\frac{k\Delta x}{2}\right) - \sin^2\left(\frac{\omega\Delta t}{2}\right) = 0, \tag{21}$$

where C_δ and C_μ are the QED parameters given in Fig. 1 as a function of the homogeneous magnetic field strength.

The modification of the X-mode dispersion relation in Eq. (21) compared to the classical one in Eq. (20) depends on $C_\mu \sin^2\theta$. Recall from Fig. 1 that the value of the parameter C_μ saturates at a value much less than 10^{-2}. This means there is no effect on the X-mode waves propagating parallel to the homogeneous magnetic field, $\theta = 0$, and a negligible modification that is much less than one percent for the ones propagating perpendicular to the homogeneous magnetic field.

For the ordinary electromagnetic mode (O mode), where the wave-like perturbation components are δB_z, δE_x, and δE_y, the dispersion relation [Eq. (B11)] gets the form

$$\left(\frac{1 - C_\delta + C_\varepsilon \cos^2\theta}{1 - C_\delta + C_\varepsilon}\right)\left(\frac{c\Delta t}{\Delta x}\right)^2 \sin^2\left(\frac{k\Delta x}{2}\right) - \sin^2\left(\frac{\omega\Delta t}{2}\right) = 0, \tag{22}$$

where C_δ and C_ε are the QED parameters given in Fig. 1 as a function of the homogeneous magnetic field strength. The QED modification of the O-mode dispersion relation is significant compared to the O mode; in Fig. 3, we see this as a severe reduction of the phase speed of the O-mode waves. Both the physical and the numerical dispersion phase speeds of the O-mode waves decrease as the homogeneous magnetic field increases and as the angle between the magnetic field and the wave vector approaches $\frac{\pi}{2}$. The numerical speed is always less than the physical light speed for the same parameters, which ensures the stability of the simulation based on the Courant–Friedrichs–Lewy condition (Courant *et al.*, 1928) for the time step size.

Note that the deviation between the physical and numerical dispersion Fig. 3 has nothing to do with the QED modification, as the same discrepancy between the two curves manifests for the weak field regime as well. We also see in Fig. 3 that the thermal speed of the particles in the performed test simulations in Sec. IV is always less than the phase speed at small wave numbers. Therefore, we do not expect any Cherenkov radiation at short wave numbers in those simulations. However, as the magnetars' magnetospheric plasma is relativistic, the expected amount of the numerical Cherenkov radiation can be higher in simulations with relativistic setups.

Because the new algorithm also interpolates grid cell points of electromagnetic fields that are further away than in the case of the second-order Yee algorithm, it increases and decreases the minimal wavelengths and wave numbers, respectively, that can be resolved. Thus, it creates a low-pass filter with a kernel size larger than in the Yee algorithm. Moreover, the kernel size increases with increasing magnetic fields as the linearly interpolated points further away contribute more for stronger fields. Nonetheless, even with this increase, we do not detect any issue in our tests because the typical wave numbers of the presented wave modes are still well resolved.

D. Simulation setup

To demonstrate the proposed field solver functionality, we implemented the numerical scheme of QED polarization into a 1D3V (one spatial dimension, three velocity components) version of our code ACRONYM (Kilian *et al.*, 2012) on the rectangular Yee grid

TABLE I. Summary of used plasma and simulation parameters.

Parameter	Value
Magnetic field intensities B/B_Q	100, 1000, and 10 000
Magnetic field angles θ	$\pi/30$, $\pi/4$, and $\pi/2$
Frequency ratio ω_c/ω_p	3
Initial thermal velocity v_t/c	0.05
Simulation length L/Δ	20 000
Simulation time $\omega_p t_{end}$	800
Skin depth resolution Δ/d_e	0.05
Time step size $\omega_p \Delta t$	0.02

Yee (1966). Though ACRONYM generally has a few high-order field solvers, our implementation is second-order. However, we utilize a high-order current-conserving deposition scheme with a fourth-order piecewise quadratic shape (PQS) function for macro-particles (Esirkepov, 2001). We use the Vay *et al.* (2011) particle pusher. No further modifications of the particle dynamics in the quantum regime are implemented. The simulation macro-particles interact with the electromagnetic fields using the classical Lorentz force.

The summary of plasma and simulation parameters is given in Table I. We carry out a series of simulations of thermal plasma in strong external magnetic fields of intensities $B/B_Q = 100$, 1000, and 10 000. In all cases, the plasma consists of electrons and positrons, and it initially has a uniform density n and is composed of a certain ratio of electrons and positrons. The used non-neutral fractions of the electrons and positrons plasma $\Delta n/n = (n_p - n_e)/n$ are 0, 0.5, and 1, where n_e is the electron density, n_p is the positron density and $n = n_e + n_p$ is the total plasma density.

The specific value of plasma density is obtained from the cyclotron to plasma frequency ratio, which we fix to a value of $\omega_c/\omega_p = 3$, where $\omega_c = eB/m_e$ is the electron cyclotron frequency. The plasma density is in all cases represented by 40 macro-particles per cell. The used ratio $\omega_c/\omega_p = 3$ is unrealistically low, producing plasma densities with particles closer to each other than the de Broglie wavelength. Nonetheless, we use this value for test purpose because the ratio (1) separates the cyclotron and plasma frequency effects sufficiently to resolve the plasma dispersion properties at both frequencies and (2) it reduces computational requirements because of the necessity to resolve the cyclotron motion as well as sufficiently long time in terms of the plasma periods.

The cyclotron period is resolved by ≈105 time steps. We also do not detect any problems with the Boris push in terms of the numerical heating or an incorrectly described particle path. In our simulations, the Larmor radius $r_c = v_t/\omega_c$ is resolved by $0.3\bar{3}\Delta$. Nonetheless, we tested a simulation with $r_c \approx 13.3\bar{3}\Delta$, $L/\Delta = 10^6$, and 10^6 time steps of 40 times better temporal resolution. Not only is the simulation stable and without generation of numerical cyclotron instabilities, but it also better conserves the total energy.

The initial thermal velocity is $v_t/c = 0.05$ with a Maxwellian velocity distribution. We consider three angles $\theta = \pi/30, \pi/4$, and $\pi/2$ between the magnetic field vector and the simulation domain x-axis, to study quasi-parallel, oblique, and perpendicular wave types. Also, the magnetic field intensities B/B_Q and propagation angles θ are selected for a comparison of analytical dispersion properties obtained in Medvedev (2023).

The simulation domain is $L = 20\ 000\Delta = 1000 d_e$ long, where $\Delta = 0.05 d_e$ is the grid cell size and $d_e = c/\omega_p$ is the plasma skin depth. The wave number resolution is $kc/\omega_p = 6.3 \times 10^{-3}$. The simulation time step is $\Delta t = 0.02\omega_p^{-1} = 0.06\omega_c^{-1}$. Therefore, the stability conditions of Eqs. (21) and (22) are fulfilled for all simulation setups. The simulation is carried out for 40 000 Δt, i.e., $\omega_p t_{end} = 800$, allowing frequency resolution of $\Delta\omega/\omega_p = 7.9 \times 10^{-3}$. We use periodic boundary conditions.

IV. RESULTS

The results of tests of plasma dispersion properties in superstrong magnetic fields are presented in Figs. 4–7. The figures are overlaid by black dashed lines representing the solution of linearized dispersion solutions for the cold plasma approach obtained in Medvedev (2023). In all the studied cases, the total energy in the simulation is conserved well with oscillation in approximately the same range as in a separate test simulation without the QED effects.

A. Plasma dispersion properties with QED polarization effects

Figure 4 shows the dispersion space of electric and magnetic field components for the case of $B/B_Q = 1000$ in the perpendicular direction to the magnetic field with a density ratio equal to one. The perpendicular direction manifests the birefringence effect between O and X modes. The E_x component shows the electrostatic cyclotron waves propagating perpendicular to the magnetic field and appearing mostly at the cyclotron frequency $\omega_c = 3\omega_p$ and its harmonics $2\omega_c$ and $3\omega_c$. The B_x component is zero throughout the simulation domain, as expected, because $\partial B_x/\partial t = \partial_y B_z - \partial_z B_y = 0$ in 1D since $\partial_y f(x) = \partial_z f(x) = 0$ for an arbitrary component of the electromagnetic fields, $f(x)$.

The dispersion branches in E_y and B_z represent the O-mode waves and E_z and B_y represent the X-mode waves. Each combination of electric and magnetic field components corresponds to the same mode. The frequency cutoff ω_{co} is the same for both components for each polarization mode. The main difference occurs close to the "light line," $\omega = kc$, for $(\omega, k) \to \infty$. When QED polarization is considered, the refractive index $N^2 = k^2c^2/\omega^2 = c^2/v_\phi^2$ of the O-mode waves increases, where v_ϕ is the phase velocity. The phase and group velocities of waves $(\omega, k) \to \infty$ decrease. For the X-mode waves, $N \approx 1$ for $(\omega, k) \to \infty$ creates the birefringence between the O and X modes. The dispersion properties of the X-mode waves do not change significantly from the non-QED approach.

The electromagnetic waves manifest increased intensity at the harmonics of the cyclotron frequency. For the harmonics that appear for the electrostatic as well as electromagnetic waves and frequencies $\omega > \omega_c$, there are no analytical solutions because they result from nonlinear wave–wave and particle–wave interactions, which are not described by the linearized analytical approach. Such nonlinear interactions are known to be present in plasmas (Melrose, 1986). However, in our case, the waves are further enhanced by numerical effects due to the finite number of particles and grid cells (Ganse *et al.*, 2012).

We do not present the results of the QED polarization solver for $B \lesssim B_Q$ because Eqs. (18) and (19) approach classical Ampère's law for $B \to 0$ and the QED polarization effects on the plasma dispersion

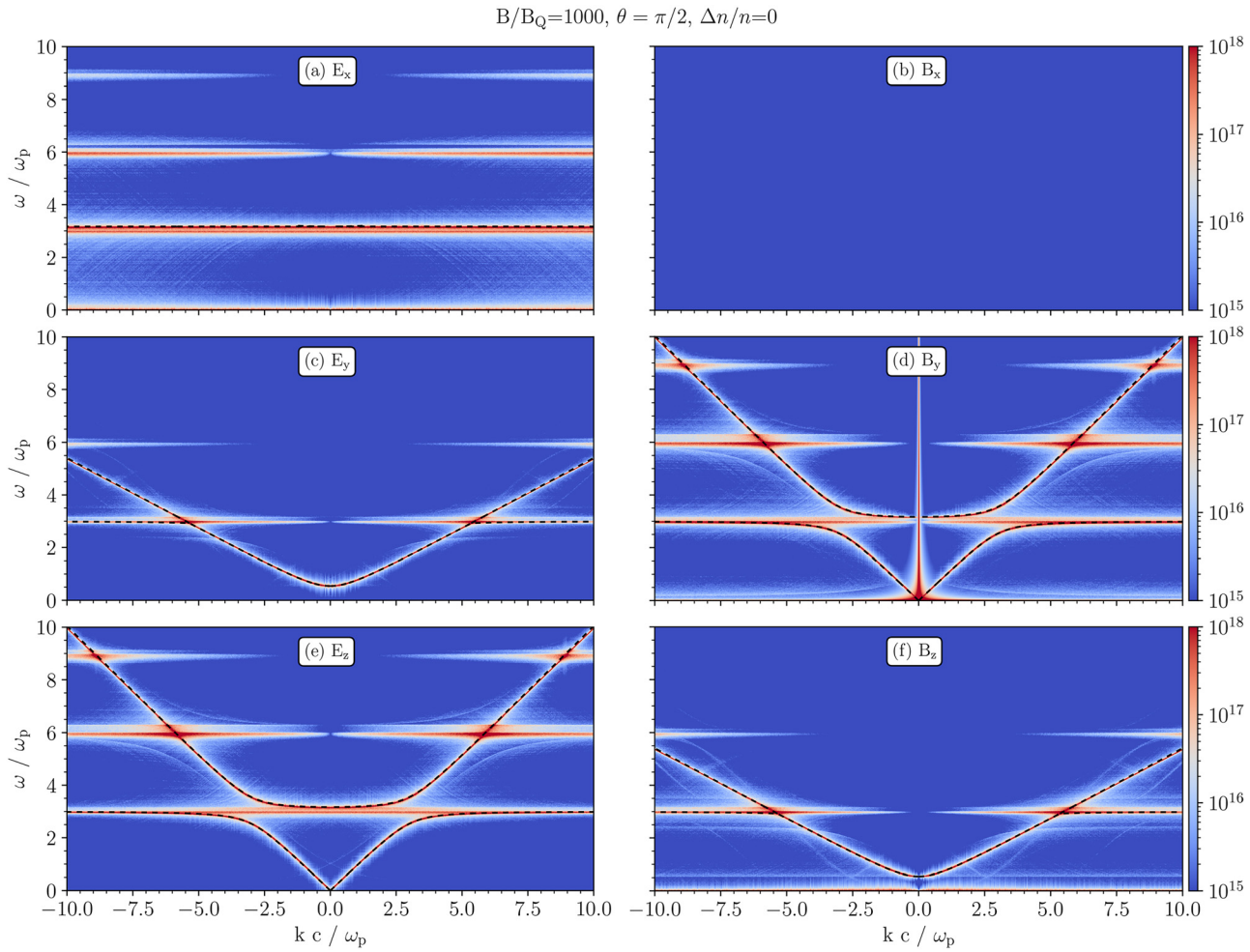

FIG. 4. The dispersion diagrams of the electric and magnetic field components show the wave birefringence between the *O* [E_y and B_z components in (c) and (f)] and *X*-mode [E_z and B_y components in (e) and (d)] waves for $B/B_Q = 1000$, $\theta = \pi/2$, and $\Delta n/n = 0$. There are present (a) electrostatic longitudinal and (b) no magnetostatic longitudinal waves.

properties will be negligible. In agreement with the analytical solution, the numerical implementation also intrinsically approaches the classical second-order Yee solver for $B \to 0$ with error down to machine precision.

B. Tests for broad plasma parameter space

We focus from now on an investigation and comparison of analytical and numeric results in a broader parameter space. The electric field dispersion properties as a function of θ are shown in Fig. 5 for an electron/positron density ratio of unity. We do not present the magnetic field components because they show the same properties. The dispersion space of the E_x component for $\theta = \pi/30$ consists mostly of quasi-parallel electrostatic Langmuir waves close to the plasma frequency; however, the electromagnetic branches are also projected into E_x. The electrostatic mode close to ω_p bends slightly to higher frequencies with increasing k, while the analytical solution does not because, in comparison with the analytical solution obtained for cold plasma, we consider plasma with thermal effects. The difference is mostly noticeable from the figures for $kc/\omega_p \sim 4 - 5$.

The Langmuir branch, located around the frequency $\sim \omega_p$ and visible in E_x and E_y, is a monotonous curve for parallel propagation and separates into two branches close to $\omega/\omega_p \approx kc/\omega_p \approx 0.6$ for an increased angle $\theta = \pi/4$. The resulting branches have superluminal and subluminal parts that do not intersect the light line $\omega = kc$. Only the electrostatic cyclotron mode appears for perpendicular waves at $\theta = \pi/2$ in E_x. The E_y component representing the *O*-mode polarized waves undergoes a decrease in the wave phase and group velocities with an increasing θ close to the light line $\omega/kc \lesssim 1$. The *X*-mode wave properties of E_z component do not significantly depend on θ.

Figure 6 shows the electric field dispersion properties for increasing magnetic field intensity from $B/B_Q = 100$ to 10 000. The component E_x is not shown because it does not have significant dependence on B and is similar to Fig. 4(a). While there are no detectable changes

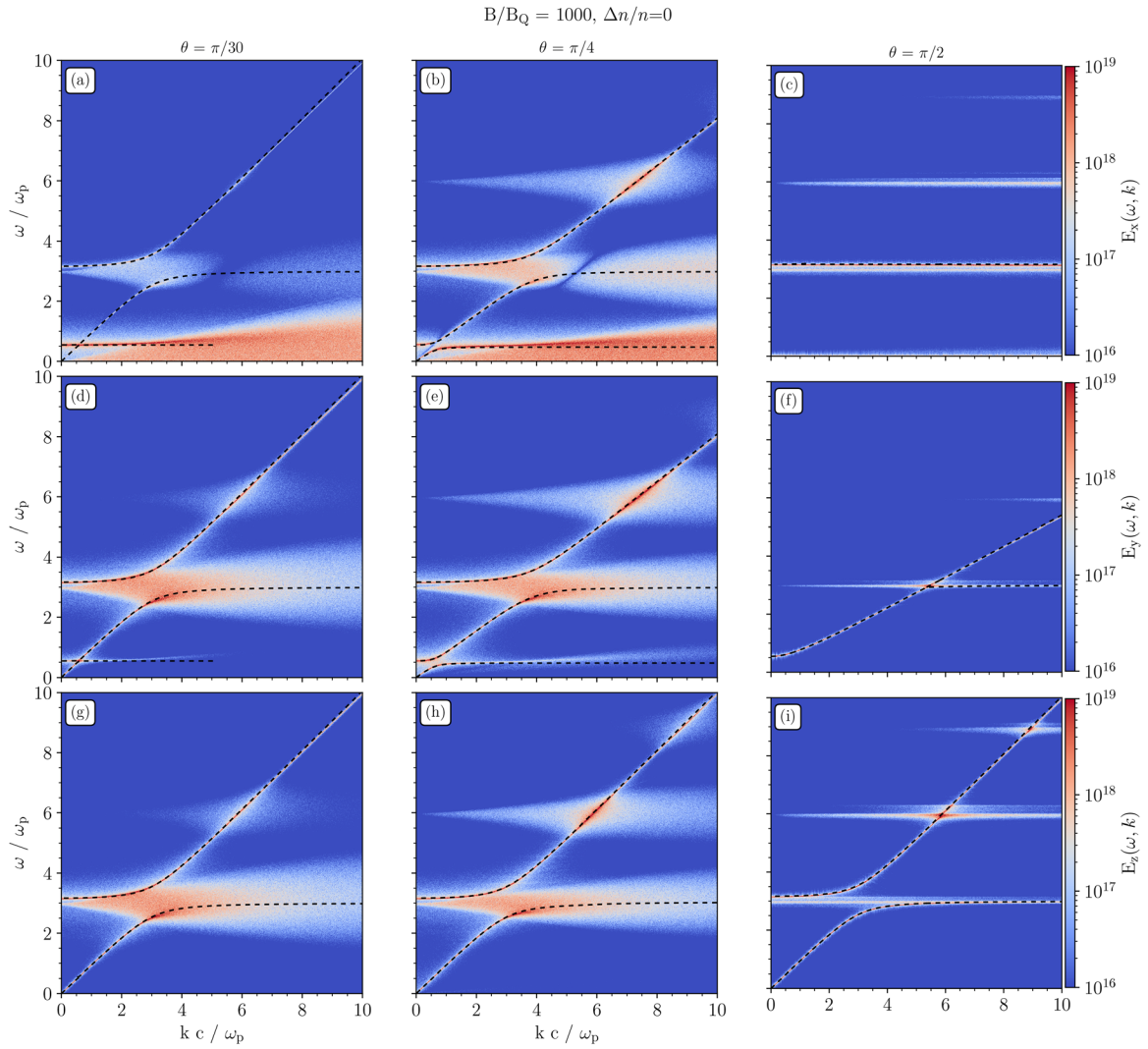

FIG. 5. The dispersion diagrams of the electric field components for changing the propagation angle to the magnetic field θ for $B/B_Q = 1000$ and $\Delta n/n = 0$. The electric field components (a)–(c) E_x, (d)–(f) E_y, and (g)–(i) E_z. The left column (a), (d), (g) is for quasi-parallel waves, the middle column (b), (e), (h), the angle $\pi/4$, and the right column (c), (f), (i) for perpendicular waves.

in E_x and E_z components, the O-mode waves in E_y bend toward lower phase velocities as expected for increasing refractive index N with increasing $\boldsymbol{B}$.

In Fig. 7, we present the dispersion properties of electrostatic waves for $\theta = \pi/30$ with increasing density difference between electrons and positrons, producing non-neutral plasmas. Such plasmas can be found in compact object magnetospheres, e.g., magnetar magnetospheres, where the plasma can reach the Goldreich–Julian (GJ) charge density. The GJ density is the minimum plasma density needed for the magnetosphere to co-rotate with a neutron star or a magnetar. Such a co-rotation is, in essence, the $E \times B$ drift of the magnetospheric plasma. Hence, this plasma is intrinsically non-neutral. The plasma screening can result in the establishment of a force-free type of magnetosphere and co-rotation of the plasma particles with the star.

Our simulations show that with the charge density increase, the electromagnetic branches split into two branches in frequency, forming two right-handed R and left-handed L, oppositely polarized degeneracies. The analytical solutions of both polarization modes are overlaid in both rows to demonstrate the differences in the positions. The analysis shows that for $\Delta n/n = 1$ the upper and lower modes above and below ω_c are the L modes and the mode close to the light line $\omega/kc = 1$ is R mode. For $\Delta n/n = 0.5$, the R mode deviates from the light line, but the R mode still stays closer to the cyclotron frequency. The position of the electrostatic Langmuir mode remains the same in all cases.

C. Kinetic effects for ground-level Landau quantization

In the quantum regime, the particle's perpendicular momenta are quantized into Landau levels. The transitions between the levels are

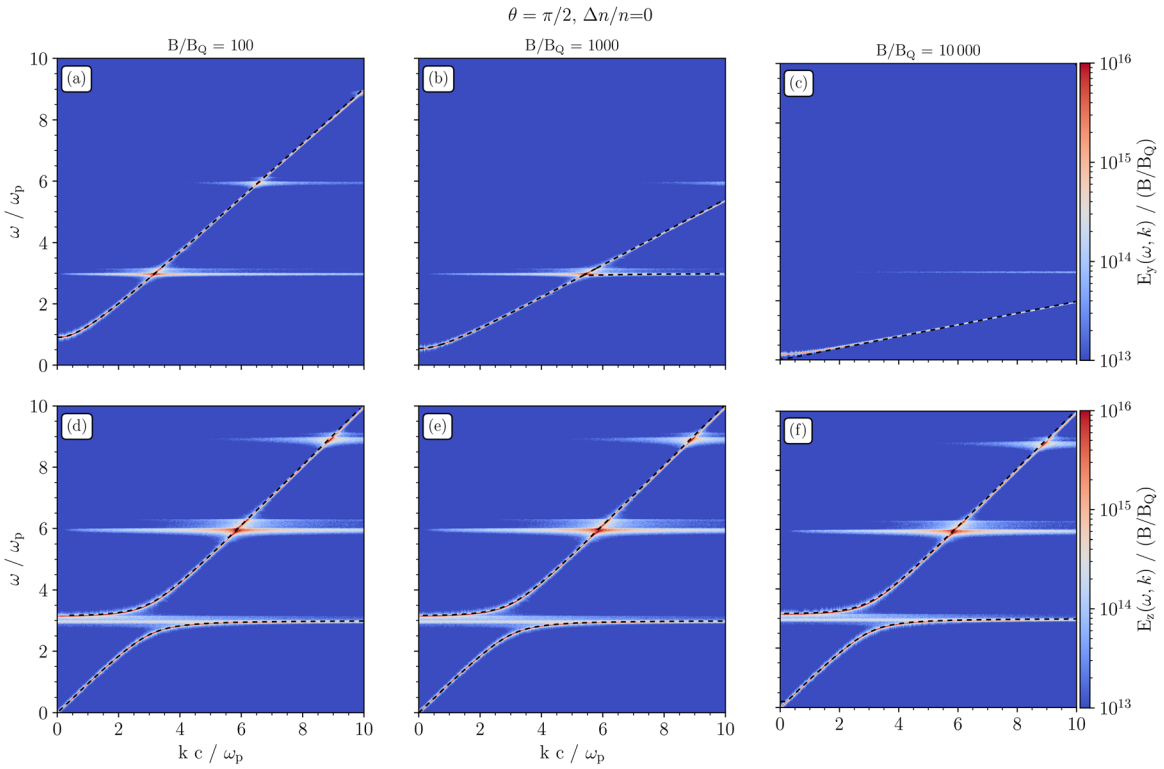

FIG. 6. The dispersion diagrams of the electric field components on the magnetic field intensity B/B_Q for $\theta = \pi/2$ and $\Delta n/n = 0$. The electric field components of electromagnetic waves (a)–(c) E_y and (d)–(f) E_z. The left column (a), (d), (g) is for B/B_Q, the middle column (b), (e), (h) for B/B_Q, and the right column (c), (f), (i) for B/B_Q.

done by absorbing or emitting a quantum of energy. Though this process is not described in the simulations, we can employ the ground level by setting the perpendicular velocity to zero, corresponding to the case that the perpendicular momenta are radiated by the cyclotron losses.

In addition, the usage of a very small ratio of $\omega_c/\omega_p = 3$ for our tests, which cannot be achieved in realistic plasma, allows us to study the dispersion properties around both the plasma frequency and the cyclotron frequency. Nonetheless, the question arises whether the solver also provides reliable outputs when $\omega_p \lll \omega_c$ in the magnetar magnetospheres or laser plasmas.

To test these aspects, we conducted two additional simulations with one-dimensional velocity distribution (1D1V) with a nonzero velocity component along the magnetic field for fixed B/B_Q, $\theta = \pi/2$, $\Delta n/n = 0$, and $v_t/c = 0.05$. In the second of these simulations, we also separated the cyclotron and frequencies by setting the ratio $\omega_c/\omega_p = 3 \times 10^5$ but adjusting the time step and grid cell sizes to resolve the processes close to the plasma frequency ($\Delta x/d_e = 0.05$ and $\Delta t\omega_p = 0.02$). Thus, the cyclotron frequency and the Larmor radius are not resolved by the time step size and the grid cell size, respectively.

The results are shown in Fig. 8 and compared with the simulation having a three-dimensional velocity distribution (1D3V). While the cyclotron effects are not well described in Fig. 8(b) and not present in Fig. 8(c), the plasma effects, as well as the QED polarization effects, are present in both cases (b–c). Therefore, the developed framework can also be utilized in simulations that resolve only the electron plasma and lower frequencies and describe the high-frequency particle Larmor motion by gyro-motion, gyro-center, or gyro-kinetic approximations.

V. DISCUSSION

Our investigation in this paper focused on reproducing the modifications in the dispersion relations of electromagnetic waves in a PIC simulation that are imposed by QED effects of the superstrong magnetic field exceeding the Schwinger limit. The newly developed solver for QED polarization reproduces birefringence effects between the O and X polarized modes. We demonstrated that the obtained dispersion properties follow the analytical solutions derived for cold plasma.

Our solver can be applied to arbitrarily strong magnetic fields because the analytical and numerical solutions approach the "classical" Maxwell equations. Our investigation and tests focused, however, on magnetic fields with $B/B_Q = 10^2 - 10^4$ because of these strengths, the deviations from classical solutions are larger than for magnetic fields around B_Q.

We find that in plasmas with nonzero charge density in the emission and propagation regions, which can be located in magnetar magnetospheres, the L and R polarized modes can be split/degenerated. This splitting could cause an observable time delay of circularly polarized waves if the waves are emitted below or close to the cyclotron frequency.

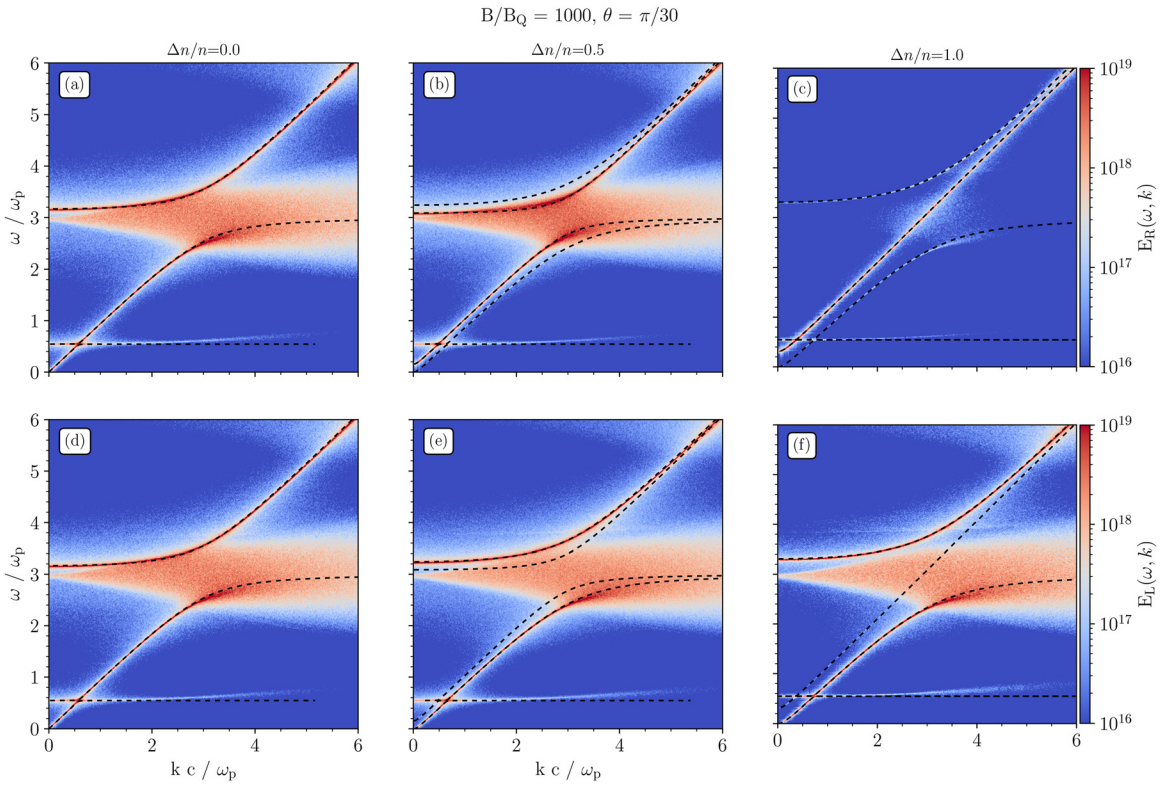

FIG. 7. The dispersion diagrams of the electric field components on the charge density imbalance $\Delta n/n = 0$ for $B/B_Q = 1000$ and $\theta = \pi/2$ separated into (a)–(c) *R* and (d)–(f) *L*-mode polarization components. The left column (a), (d), (g) is for a zero net charge $\Delta n/n = 0$, the middle column (b), (e), (h) for $\Delta n/n = 0.5$, and the right column (c), (f), (i) for a purely positron plasma $\Delta n/n = 1$.

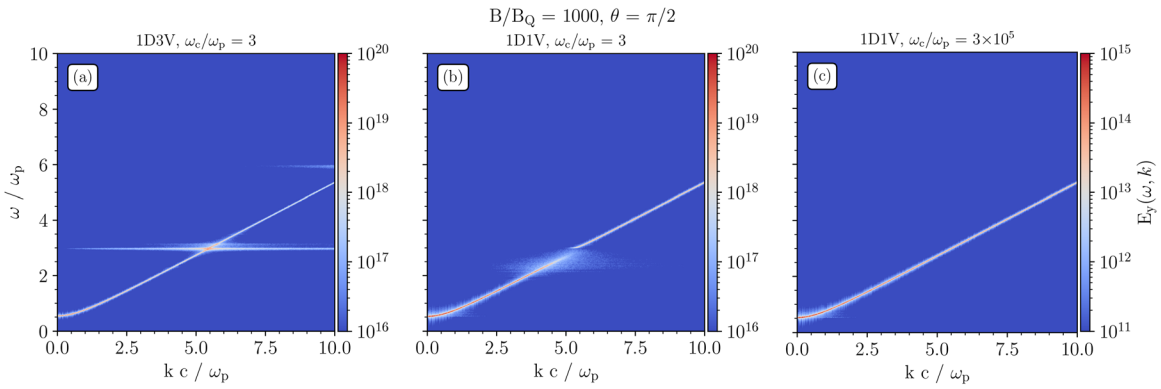

FIG. 8. Comparison of the dispersion properties of the E_y component for (a) three-dimensional (1D3V) (b) one-dimensional (1D1V) velocity distribution, and (c) plasma frequency decreased by five orders of magnitude, demonstrating in (c) the advantage of the QED polarization solver in the case of unresolved cyclotron frequency in the gyromotion, gyro-center, and gyro-kinetic approximations. The other parameters are fixed to B/B_Q, $\theta = \pi/2$, $\Delta n/n = 0$, and $v_t/c = 0.05$.

A. Thermal effects in plasma

One of the main advantages of introducing the electromagnetic-field solver for QED polarization is its ability to be exploited for kinetic plasma simulations. The kinetic simulations, as opposed to nonlinear Maxwell equations alone, can self-consistently describe nonlinear wave–wave and particle–wave effects and also the time evolution of plasma instabilities. In addition, the kinetic simulations can deal with finite-temperature modifications of the dispersion properties.

The thermal effects are one of the reasons for differences between the analytically derived and simulated dispersion relations. Among

other differences is the numerical bending of the light line in the frequency/wave-number space toward lower frequencies at high ω and high k, which can potentially cause numerical Cerenkov radiation if particles with a speed close to the light speed are present in the simulation. However, our results show that the numerical Cerenkov radiation in our implementation is comparable with that seen with the classical second-order non-QED field solver.

Another difference between analytical and numerical solutions is for the electrostatic Langmuir branch, which is located around $\omega/\omega_p \lesssim 1$ and bends toward higher frequencies with increasing wave number. The difference between the solution is mostly seen in Figs. 5(a), 5(b), and 7 around $kc/\omega_p \approx 4$.

B. Advantages and limitations of the QED polarization approach

There are a few effects of very strong magnetic fields that our simulation cannot capture. Cyclotron radiation is a significant cooling mechanism for electrons in superstrong magnetic fields, and most of the plasma energy can be released as electromagnetic radiation due to the extremely fast gyration of the electrons. For electrons, the ratio of the cyclotron cooling time, $\tau_{cyc,cool}$, with the Larmor gyration time, τ_g, is

$$\frac{\tau_{cyc,cool}}{\tau_g} = \frac{9}{16\pi\alpha}\left(\frac{B_Q}{B}\right), \tag{23}$$

where α is the fine-structure constant. Equation (23) yields a timescale ratio of 0.25 for a magnetic field a hundred times as strong as the critical field.

In physical systems, this implies a substantial energy loss due to radiation, but in our test simulations, the effect is absent because periodic boundary conditions conserve the total energy of the system. The emitted electromagnetic waves cannot escape and are reabsorbed, leading to an equilibrium between particles and fields. This explains why, in contrast to physical expectations, the particle distribution function in the perpendicular direction remains nearly constant throughout the simulation time.

Furthermore, the quantum nature of particles becomes important when the particle separation is smaller or comparable to the De Broglie wavelength, $\lambda_{dB} = \frac{h}{m_e v_{th}} \sim 7.8 \times 10^{-10}$ cm, where the particle velocity is taken as the thermal velocity in the test simulations, $v_{th} = 0.05c$. This condition is satisfied for a density of 2.1×10^{27} cm^{-3} or higher. Even though this critical density is much higher than the typical plasma densities around the neutron star's surface, $10^{12} - 10^{18}$ cm^{-3}, we reach densities in the test simulations for which the wave-like nature of particles is important. The reason is that we require a fixed frequency ratio of $\omega_c/\omega_p = 3$ to compare with the analytically derived dispersion curves. For example, for a magnetic strength of $10^4 B_Q$, the implied plasma density is around 5×10^{39} cm^{-3}, which is far higher than the critical density of 2.1×10^{27} cm^{-3}.

This highlights a further limitation of our test setup; to maintain analytical comparability, we must work in an unphysical density regime where the quantum wave nature of particles should, in principle, be included. While the QED polarization solver itself is independent of particle quantization, the background plasmas are not. Thus, our test results should be interpreted primarily as a validation of the field solver rather than as a fully realistic model of magnetized pair plasma.

In this context, it is important to note also that the applicability of the classical PIC description itself becomes questionable as the magnetic field approaches the critical strength. In this regime, the particle energy states are Landau-quantized, lacking a well-defined perpendicular momentum to the magnetic field, with an uncertainty on the perpendicular momentum of the order of mc for a single energy eigenstate. A quantum kinetic treatment based on the Dirac equation (Al-Naseri *et al.*, 2020) showed that the dynamics in ultrastrong magnetic fields can still, to a large extent, be approximated by a classical picture if each particle is assigned an effective mass corresponding to its Landau level. This suggests that our PIC scheme may remain approximately valid, but deviations are expected depending on the physical setup (Brodin and Al-Naseri, 2024). In our present tests, we deliberately neglect Landau quantization and treat particles as classical, or we assume particles in the ground Landau level. This is an explicit limitation of the model, which would require a fully quantum kinetic extension for self-consistent studies in the $B \sim B_Q$ regime.

We note that our present PIC implementation does not include particle spin dynamics. Recent advances have shown, however, that spin effects can play a non-negligible role in wave–particle interactions (Manfredi *et al.*, 2019). Crouseilles *et al.* (2021) developed a geometric PIC scheme for the spin Vlasov–Maxwell system. Their PIC code was tested with the Raman scattering of an electromagnetic wave on an underdense plasma. More recently, Crouseilles *et al.* (2023) analyzed both scalar and vectorial spin-Vlasov–Maxwell models and showed that terms involving second-order mixed derivatives in momentum and spin cannot be treated within the PIC framework. While spin effects are beyond the scope of the present work, their inclusion would be a natural extension of our approach, potentially leading to a more complete description of plasma dynamics in extreme magnetic fields.

Another effect not yet included in our present approach is photon annihilation with the magnetic field, which can generate new pairs. Nevertheless, the newly developed numerical field solver for QED polarization represents a significant step forward; it provides a robust and versatile foundation upon which a fully self-consistent kinetic model of plasma in ultra-strong magnetic fields can be built.

VI. CONCLUSIONS

To model magnetic fields exceeding the Schwinger limit, we developed a field solver including QED polarization and implemented it in a PIC plasma code. With this extension, the PIC code allows us to investigate arbitrarily strong magnetic fields, including the superstrongly magnetized plasma environments at kinetic scales, as found in the magnetospheres of magnetars or in laboratory plasma experiments with lasers. The advantages of the solver are (1) the applicability for gyro-motion, gyro-center, and gyro-kinetic simulations, which do not resolve the cyclotron motion, (2) the possibility to study plasmas with relativistic temperatures present in, e.g., magnetar magnetospheres and laser plasmas using the PIC method, and (3) to describe the nonlinear evolution of systems harboring time- and spatially-dependent electromagnetic fields in vacuum and plasmas.

The field solver for QED polarization well reproduces the dispersion properties of electrostatic and electromagnetic waves in cold plasma that were derived in Medvedev (2023). The *O*- and *X*-mode polarizations show birefringence, which increases with increasing magnetic-field intensity and could explain the polarization properties

of high-energy radiation observed from magnetars. In addition, the R and L polarizations split into two modes for plasma with a nonzero net charge density, which can be found around magnetars. The full consideration of QED particle effects in ultra-strong magnetic fields is nontrivial to implement.

The main limitation of our approach is the consideration of a full three-dimensional velocity space of particles (1D3V) and a space in which all particles are in the ground Landau level (1D1V). In our future work, we would like to tackle the particle effects by implementing QED effects in the numerical plasma macroparticles, and utilization of the code for studying electromagnetic instabilities in magnetar magnetospheres.

ACKNOWLEDGMENTS

We thank Andrew Taylor for the helpful discussion and comments. We thank the reviewers for their valuable comments and constructive feedback, which greatly improved the quality of this paper. We acknowledge the developers of the ACRONYM code (Verein zur Förderung kinetischer Plasmasimulationen e.V.). We acknowledge the support of the German Science Foundation (DFG) project BE 7886/2-1. M.M. acknowledges support by NSF via Grant No. PHY-2409249. The authors gratefully acknowledge the Gauss Center for Supercomputing e.V. (www.gauss-centre.eu) for partially funding this project by providing computing time on the GCS Supercomputer Super-MUC-NG at Leibniz Supercomputing Center (www.lrz.de), project pn72ku.

AUTHOR DECLARATIONS

Conflict of Interest

The authors have no conflicts to disclose.

Author Contributions

M. Alawashra and J. Benáček contributed equally to this work.

M. Alawashra: Conceptualization (equal); Formal analysis (equal); Methodology (equal); Validation (equal); Visualization (equal); Writing – original draft (equal). **J. Benáček:** Conceptualization (equal); Formal analysis (equal); Methodology (equal); Validation (equal); Visualization (equal); Writing – original draft (equal). **M. Pohl:** Supervision (equal); Writing – review & editing (lead). **M. V. Medvedev:** Data curation (supporting); Writing – review & editing (supporting).

DATA AVAILABILITY

The data that support the findings of this study are available from the corresonding author upon reasonable request. The numerical code he QED field solver is available at the Zenodo platform at https://doi.org/10.5281/zenodo.15004304, Alawashra *et al.* (2025).

APPENDIX A: FIELD SOLVER FOR QED POLARIZATION

Here, we derive the explicit electric fields' time derivatives for the modified Ampère's law in the superstrong magnetic fields approach [Eq. (15)]. We start by expressing the QED parameters (C_δ, C_μ, and C_ε) as given by Eqs. (10)–(12). Then, we rearrange the equations of the spatial components of Eq. (15) in the following matrix form:

$$\begin{bmatrix} A_{xx} & A_{xy} & A_{xz} \\ A_{yx} & A_{yy} & A_{yz} \\ A_{zx} & A_{zy} & A_{zz} \end{bmatrix} \begin{bmatrix} \frac{\partial E_x}{\partial t} \\ \frac{\partial E_y}{\partial t} \\ \frac{\partial E_z}{\partial t} \end{bmatrix} = \begin{bmatrix} \frac{1}{c} j_x - Q_x \\ \frac{1}{c} j_y - Q_y \\ \frac{1}{c} j_z - Q_z \end{bmatrix}, \tag{A1}$$

where the components of the matrix A are given by

$$A_{ij} = \frac{1}{c}\left[\gamma_{\mathscr{F}}\delta_{ij} - \gamma_{\mathscr{F}\mathscr{F}} E_i E_j - \gamma_{\mathscr{G}\mathscr{G}} B_i B_j\right], \tag{A2}$$

with i and j looping over the spatial coordinates x, y, and z. Here j_x, j_y, and j_z are the spatial components of the electric current. The additional Q terms on the right-hand side include all the spatial derivatives of the electric and magnetic fields, along with the time derivatives of the magnetic fields and are given as

$$\begin{aligned} Q_x = {} & \gamma_{\mathscr{F}}\left[-\left(\frac{\partial B_z}{\partial y} - \frac{\partial B_y}{\partial z}\right)\right] + \gamma_{\mathscr{F}\mathscr{F}}\left[\frac{1}{c}E_x\left(\mathbf{B}\cdot\frac{\partial \mathbf{B}}{\partial t}\right)\right. \\ & + B_y\left(\mathbf{B}\cdot\frac{\partial \mathbf{B}}{\partial z} - \mathbf{E}\cdot\frac{\partial \mathbf{E}}{\partial z}\right) - B_z\left(\mathbf{B}\cdot\frac{\partial \mathbf{B}}{\partial y} - \mathbf{E}\cdot\frac{\partial \mathbf{E}}{\partial y}\right)\Big] \\ & + \gamma_{\mathscr{G}\mathscr{G}}\left[-\frac{1}{c}B_x\left(\mathbf{E}\cdot\frac{\partial \mathbf{B}}{\partial t}\right) + E_y\left(\mathbf{E}\cdot\frac{\partial \mathbf{B}}{\partial z} + \mathbf{B}\cdot\frac{\partial \mathbf{E}}{\partial z}\right)\right. \\ & \left. - E_z\left(\mathbf{E}\cdot\frac{\partial \mathbf{B}}{\partial y} - \mathbf{B}\cdot\frac{\partial \mathbf{E}}{\partial y}\right)\right], \end{aligned} \tag{A3}$$

$$\begin{aligned} Q_y = {} & \gamma_{\mathscr{F}}\left[-\left(\frac{\partial B_x}{\partial z} - \frac{\partial B_z}{\partial x}\right)\right] + \gamma_{\mathscr{F}\mathscr{F}}\left[\frac{1}{c}E_y\left(\mathbf{B}\cdot\frac{\partial \mathbf{B}}{\partial t}\right)\right. \\ & + B_z\left(\mathbf{B}\cdot\frac{\partial \mathbf{B}}{\partial x} - \mathbf{E}\cdot\frac{\partial \mathbf{E}}{\partial x}\right) - B_x\left(\mathbf{B}\cdot\frac{\partial \mathbf{B}}{\partial z} - \mathbf{E}\cdot\frac{\partial \mathbf{E}}{\partial z}\right)\Big] \\ & + \gamma_{\mathscr{G}\mathscr{G}}\left[-\frac{1}{c}B_y\left(\mathbf{E}\cdot\frac{\partial \mathbf{B}}{\partial t}\right) + E_z\left(\mathbf{E}\cdot\frac{\partial \mathbf{B}}{\partial x} + \mathbf{B}\cdot\frac{\partial \mathbf{E}}{\partial x}\right)\right. \\ & \left. - E_x\left(\mathbf{E}\cdot\frac{\partial \mathbf{B}}{\partial z} - \mathbf{B}\cdot\frac{\partial \mathbf{E}}{\partial z}\right)\right], \end{aligned} \tag{A4}$$

and

$$\begin{aligned} Q_z = {} & \gamma_{\mathscr{F}}\left[-\left(\frac{\partial B_y}{\partial x} - \frac{\partial B_x}{\partial y}\right)\right] + \gamma_{\mathscr{F}\mathscr{F}}\left[\frac{1}{c}E_z\left(\mathbf{B}\cdot\frac{\partial \mathbf{B}}{\partial t}\right)\right. \\ & + B_x\left(\mathbf{B}\cdot\frac{\partial \mathbf{B}}{\partial y} - \mathbf{E}\cdot\frac{\partial \mathbf{E}}{\partial y}\right) - B_y\left(\mathbf{B}\cdot\frac{\partial \mathbf{B}}{\partial x} - \mathbf{E}\cdot\frac{\partial \mathbf{E}}{\partial x}\right)\Big] \\ & + \gamma_{\mathscr{G}\mathscr{G}}\left[-\frac{1}{c}B_z\left(\mathbf{E}\cdot\frac{\partial \mathbf{B}}{\partial t}\right) + E_x\left(\mathbf{E}\cdot\frac{\partial \mathbf{B}}{\partial y} + \mathbf{B}\cdot\frac{\partial \mathbf{E}}{\partial y}\right)\right. \\ & \left. - E_y\left(\mathbf{E}\cdot\frac{\partial \mathbf{B}}{\partial x} - \mathbf{B}\cdot\frac{\partial \mathbf{E}}{\partial x}\right)\right]. \end{aligned} \tag{A5}$$

Finally, multiplying Eq. (A1) with A^{-1} we get the explicit form of the electric field temporal evolution

$$\frac{\partial \mathbf{E}}{\partial t} = A^{-1}\left(\frac{1}{c}\mathbf{j} - \mathbf{Q}\right), \tag{A6}$$

where

$$A^{-1} = \frac{1}{|A|}\begin{bmatrix} A_{yy}A_{zz} - A_{zy}A_{yz} & A_{xz}A_{zy} - A_{zz}A_{xy} & A_{xy}A_{yz} - A_{yy}A_{xz} \\ A_{yz}A_{zx} - A_{zz}A_{yx} & A_{xx}A_{zz} - A_{zx}A_{xz} & A_{xz}A_{yx} - A_{yz}A_{xx} \\ A_{yx}A_{zy} - A_{zx}A_{yy} & A_{xy}A_{zx} - A_{zy}A_{xx} & A_{xx}A_{yy} - A_{yx}A_{xy} \end{bmatrix}, \tag{A7}$$

and

$$|A| = A_{xx}(A_{yy}A_{zz} - A_{zy}A_{yz}) - A_{xy}(A_{yx}A_{zz} - A_{zx}A_{yz}) + A_{xz}(A_{yx}A_{zy} - A_{zx}A_{yy}). \tag{A8}$$

1. Implementation in 1D3V PIC

When implementing the QED polarization solver [Eq. (A6)] in a 1D3V PIC code (one spatial dimension, three velocity and electromagnetic field components), the only part that is changed is the **Q** vector. If we have the simulation spatial extent in the x-axis, then we get the following expressions for the components of the **Q** vector

$$Q_x = \gamma_{\mathscr{F}\mathscr{F}}\left[\frac{1}{c}E_x\left(\mathbf{B}\cdot\frac{\partial \mathbf{B}}{\partial t}\right)\right] + \gamma_{\mathscr{G}\mathscr{G}}\left[-\frac{1}{c}B_x\left(\mathbf{E}\cdot\frac{\partial \mathbf{B}}{\partial t}\right)\right], \tag{A9}$$

$$Q_y = \gamma_{\mathscr{F}}\left[\left(\frac{\partial B_z}{\partial x}\right)\right] + \gamma_{\mathscr{F}\mathscr{F}}\left[\frac{1}{c}E_y\left(\mathbf{B}\cdot\frac{\partial \mathbf{B}}{\partial t}\right) + B_z\left(\mathbf{B}\cdot\frac{\partial \mathbf{B}}{\partial x} - \mathbf{E}\cdot\frac{\partial \mathbf{E}}{\partial x}\right)\right] + \gamma_{\mathscr{G}\mathscr{G}}\left[-\frac{1}{c}B_y\left(\mathbf{E}\cdot\frac{\partial \mathbf{B}}{\partial t}\right) + E_z\left(\mathbf{E}\cdot\frac{\partial \mathbf{B}}{\partial x} + \mathbf{B}\cdot\frac{\partial \mathbf{E}}{\partial x}\right)\right], \tag{A10}$$

and

$$Q_z = \gamma_{\mathscr{F}}\left[-\left(\frac{\partial B_y}{\partial x}\right)\right] + \gamma_{\mathscr{F}\mathscr{F}}\left[\frac{1}{c}E_z\left(\mathbf{B}\cdot\frac{\partial \mathbf{B}}{\partial t}\right) - B_y\left(\mathbf{B}\cdot\frac{\partial \mathbf{B}}{\partial x} - \mathbf{E}\cdot\frac{\partial \mathbf{E}}{\partial x}\right)\right] + \gamma_{\mathscr{G}\mathscr{G}}\left[-\frac{1}{c}B_z\left(\mathbf{E}\cdot\frac{\partial \mathbf{B}}{\partial t}\right) - E_y\left(\mathbf{E}\cdot\frac{\partial \mathbf{B}}{\partial x} - \mathbf{B}\cdot\frac{\partial \mathbf{E}}{\partial x}\right)\right]. \tag{A11}$$

For the magnetic field time derivative in the calculations of the **Q** components [Eqs. (A9)–(A11)] we substitute its value from Faraday's law

$$\frac{\partial \mathbf{B}}{\partial t} = -c\nabla\times\mathbf{E} = \left(0, c\frac{\partial E_z}{\partial x}, -c\frac{\partial E_y}{\partial x}\right). \tag{A12}$$

Arriving at expressions for the **Q** vector components dependent only on the electromagnetic fields' spatial derivatives.

APPENDIX B: NUMERICAL STABILITY OF NONLINEAR MAXWELL EQUATIONS

Here, we drive the numerical dispersion relation of a wave propagating on a one-dimensional Yee grid following the nonlinear Maxwell equations. Assuming a homogeneous superstrong magnetic field in the (x,y) plane, $\mathbf{B_0} = B_0\cos\theta\hat{x} + B_0\sin\theta\hat{y}$ and wave-like perturbations in electric and magnetic fields, we find the numerical dispersion relation for two different electromagnetic wave modes (X and O modes).

For the X mode, we have the following wave-like perturbations of the fields

$$\delta\mathbf{B} = \delta\mathbf{B}_0\exp\{i(\omega\Delta t - k_x\Delta x)\}, \tag{B1}$$

$$\delta\mathbf{E} = \delta\mathbf{E}_0\exp\{i(\omega\Delta t - k_x\Delta x)\}, \tag{B2}$$

with the components δB_y, δE_x, and δE_z being nonzero and the rest of the field components vanishing.

Using the y spatial component of Faraday law [Eq. (17)], we get the following relation between δB_y and δE_z:

$$\delta B_y = -\left(\frac{c\Delta t}{\Delta x}\right)\frac{\sin\left(\frac{k\Delta x}{2}\right)}{\sin\left(\frac{\omega\Delta t}{2}\right)}\delta E_z. \tag{B3}$$

Using the QED-modified Ampère's law [Eq. (15)], we get from the z component the following relation:

$$\left[\left(\frac{1}{c}i\frac{\sin\left(\frac{\omega\Delta t}{2}\right)}{\Delta t/2}\delta E_z + i\frac{\sin\left(\frac{k_x\Delta x}{2}\right)}{\Delta x/2}\delta B_y\right)\times\left(\gamma_{\mathscr{F}} + \gamma_{\mathscr{F}\mathscr{F}}\left(\delta\mathbf{B}^2 + \delta\mathbf{B}\cdot\mathbf{B_0} - \delta\mathbf{E}^2\right)\right) + \left(i\frac{\sin\left(\frac{k_x\Delta x}{2}\right)}{\Delta x/2}B_{y0}\right)\times\left(\gamma_{\mathscr{F}\mathscr{F}}\left(\delta\mathbf{B}^2 + \delta\mathbf{B}\cdot\mathbf{B_0} - \delta\mathbf{E}^2\right)\right) + \gamma_{\mathscr{G}\mathscr{G}}\left(\frac{1}{c}i\frac{\sin\left(\frac{\omega\Delta t}{2}\right)}{\Delta t/2}\delta B_z - i\frac{\sin\left(\frac{k_x\Delta x}{2}\right)}{\Delta x/2}\delta E_y\right)\times(-\mathbf{B_0}\cdot\delta\mathbf{E} - 2\delta\mathbf{B}\cdot\delta\mathbf{E}) + \gamma_{\mathscr{G}\mathscr{G}}\left(\frac{1}{c}i\frac{\sin\left(\frac{\omega\Delta t}{2}\right)}{\Delta t/2}B_{z0}\right)(-\mathbf{B_0}\cdot\delta\mathbf{E} - 2\delta\mathbf{B}\cdot\delta\mathbf{E})\right] = 0, \tag{B4}$$

where $\gamma_{\mathscr{F}} = -(1 - C_\delta)/(4\pi)$, $\gamma_{\mathscr{F}\mathscr{F}} = C_\mu/(4\pi B^2)$, and $\gamma_{\mathscr{G}\mathscr{G}} = C_\epsilon/(4\pi B^2)$. Assuming that the wave-like perturbations always stay much smaller than the homogeneous superstrong magnetic field, $\delta B, \delta E \ll B_0$, then we neglect the terms of the orders $\delta B/B_0$, $\delta E/B_0$, $(\delta B/B_0)^2$, and $(\delta E/B_0)^2$, and keep the terms of the order of δB and δE arriving at the following relation:

$$\left[\gamma_{\mathscr{F}}\left(\frac{1}{c}\frac{\sin\left(\frac{\omega\Delta t}{2}\right)}{\Delta t}\delta E_z + \frac{\sin\left(\frac{k_x\Delta x}{2}\right)}{\Delta x}\delta B_y\right) + \gamma_{\mathscr{F}\mathscr{F}}\frac{\sin\left(\frac{k_x\Delta x}{2}\right)}{\Delta x}B_{y0}(\delta\mathbf{B}\cdot\mathbf{B_0}) - \gamma_{\mathscr{G}\mathscr{G}}\frac{1}{c}\frac{\sin\left(\frac{\omega\Delta t}{2}\right)}{\Delta t}B_{z0}(\mathbf{B_0}\cdot\delta\mathbf{E})\right] = 0. \tag{B5}$$

Substituting the perturbation components for the X-mode, we get

$$\gamma_{\mathscr{F}}\left(\frac{1}{c}\frac{\sin\left(\frac{\omega\Delta t}{2}\right)}{\Delta t}\delta E_{z0} + \frac{\sin\left(\frac{k_x\Delta x}{2}\right)}{\Delta x}\delta B_{y0}\right) + \gamma_{\mathscr{F}\mathscr{F}}\frac{\sin\left(\frac{k_x\Delta x}{2}\right)}{\Delta x}B_0^2\sin^2\theta\delta B_y = 0, \tag{B6}$$

where θ is the angle of the magnetic field with the wave propagation direction (fixed to the x-axis). Substituting Eq. (B3) in Eq. (B6), we finally find the dispersion relation for the X-mode waves

$$\left(\frac{1-C_\delta-C_\mu\sin^2\theta}{1-C_\delta}\right)\left(\frac{c\Delta t}{\Delta x}\right)^2\sin^2\left(\frac{k\Delta x}{2}\right)-\sin^2\left(\frac{\omega\Delta t}{2}\right)=0. \tag{B7}$$

Now, we go back to the O-mode waves, which have the wave-like components δB_z, δE_x, and δE_y being nonzero and the rest of the field components vanishing. Using the QED-modified Ampère's law [Eq. (15)], we get from the y component the following relation:

$$\gamma_F\left(\frac{1}{c}\frac{\sin\left(\frac{\omega\Delta t}{2}\right)}{\Delta t}\delta E_y-\frac{\sin\left(\frac{k_x\Delta x}{2}\right)}{\Delta x}\delta B_z\right)-\gamma_{gg}\frac{1}{c}\frac{\sin\left(\frac{\omega\Delta t}{2}\right)}{\Delta t}B_0\sin\theta\left(B_0\cos\theta\delta E_x+B_0\sin\theta\delta E_y\right)=0, \tag{B8}$$

and the following relation from the x component:

$$\delta E_x=\frac{\gamma_{gg}B_0^2\cos\theta\sin\theta}{\gamma_F-\gamma_{gg}B_0^2\cos^2\theta}\delta E_y. \tag{B9}$$

We also get a third relation from the z component of the Faraday's law [Eq. (17)]

$$\delta B_z=\left(\frac{c\Delta t}{\Delta x}\right)\frac{\sin\left(\frac{k\Delta x}{2}\right)}{\sin\left(\frac{\omega\Delta t}{2}\right)}\delta E_y. \tag{B10}$$

Finally, after substituting the Eqs. (B9) and (B10), in Eq. (B8), we get the dispersion relation for the O-mode waves that is

$$\left(\frac{1-C_\delta+C_\varepsilon\cos^2\theta}{1-C_\delta+C_\varepsilon}\right)\left(\frac{c\Delta t}{\Delta x}\right)^2\sin^2\left(\frac{k\Delta x}{2}\right)-\sin^2\left(\frac{\omega\Delta t}{2}\right)=0. \tag{B11}$$

APPENDIX C: NUMERICAL ALGORITHM

1. Standard Yee solver

The standard second-order explicit solver on uniform rectangular Yee grid updates the electric fields from time step n to time step $n+1$ in two steps, with an auxiliary vector array $\mathbf{E}'_{n+1}$:

1. $\mathbf{E}_n \to \mathbf{E}'_{n+1}$ by $\nabla\times\mathbf{B}_{n+\frac{1}{2}}$.
2. $\mathbf{E}'_{n+1} \to \mathbf{E}_{n+1}$ by adding electric current $\mathbf{j}_{n+\frac{1}{2}}$.

2. Solver with QED polarization effects

The new algorithm consists of a few more steps. It contains additional vector arrays of auxiliary variables $\mathbf{E}_{n+\frac{1}{2}}$, $\mathbf{E}_{n+\frac{3}{2}}$, and $\mathbf{Q}_{n+\frac{1}{2}}$ and an auxiliary matrix array $\mathbf{A}_{n+\frac{1}{2}}$. Unlike the classical Yee algorithm, the new algorithm advances each component of the electric field E^α, $\alpha=1,2,3$, separately by using the linearly interpolated values of all the electric and magnetic field components at the spatial position of the component, E^α. The new algorithm steps are summarized as follows:

1. Predict $\mathbf{E}_{n+\frac{1}{2}}$ linearly from $\mathbf{E}_n$ and $\mathbf{E}_{n-1}$.
2. Calculate coefficients $\gamma_{\mathscr{F}}$, $\gamma_{\mathscr{F}\mathscr{F}}$, and $\gamma_{\mathscr{G}\mathscr{G}}$ based on $\mathbf{B}_{n+\frac{1}{2}}$.
3. Build the matrix $A_{n+\frac{1}{2}}$ via Eq. (19) using $\mathbf{B}_{n+\frac{1}{2}}$ and $\mathbf{E}_{n+\frac{1}{2}}$; invert to get $A^{-1}_{n+\frac{1}{2}}$.
4. Calculate $Q_{n+\frac{1}{2}}$ via Eqs. (A9)–(A11) from $\mathbf{E}_{n+\frac{1}{2}}$ and $\mathbf{B}_{n+\frac{1}{2}}$.
5. Update $\mathbf{E}^\alpha_n \to \mathbf{E}^\alpha_{n+1}$ by solving Eq. (18) and using $A^{-1}_{n+\frac{1}{2}}$, $\mathbf{j}_{n+\frac{1}{2}}$, and $\mathbf{Q}_{n+\frac{1}{2}}$.
6. Predict $\mathbf{E}^\alpha_{n+\frac{3}{2}}$ linearly from $\mathbf{E}^\alpha_n$ and $\mathbf{E}^\alpha_{n+1}$.

We found that making the linear predictor in the steps 1 and 6 by using directly the difference between $\mathbf{E}^\alpha_n$ and $\mathbf{E}^\alpha_{n+1}$ conserves the field energy better than by making a prediction for $\mathbf{E}^\alpha_{n+\frac{3}{2}}$ from time $\mathbf{E}^\alpha_{n+1}$ using the classical second-order Yee scheme. Other authors and applications use this latter approach for $B\sim B_Q$ (Grismayer *et al.*, 2021; Zhang *et al.*, 2025).

The new scheme slows down the electromagnetic field solver by a factor of a few. However, since the field solver covers only a few tens of percent of the total computational requirements of the PIC code for one time step (assuming ∼100 PPC and the second-order particle shape function), the total simulation time increases by a factor of about two. Our scheme approaches the classical Yee scheme above for $B\to 0$.

REFERENCES

Alawashra, M. *et al.*, see https://doi.org/10.5281/zenodo.15004304 for "Electromagnetic field solver for QED polarization in super-strong magnetic fields of magnetar and laser plasmas" (2025).

Al-Naseri, H., Zamanian, J., Ekman, R., and Brodin, G., "Kinetic theory for spin-1/2 particles in ultrastrong magnetic fields," Phys. Rev. E **102**, 043203 (2020).

Blinne, A., Gies, H., Karbstein, F., Kohlfürst, C., and Zepf, M., "All-optical signatures of quantum vacuum nonlinearities in generic laser fields," Phys. Rev. D **99**, 016006 (2019).

Borysova, M. and On Behalf of LUXE, "Studies of high-field QED with the LUXE experiment at the European XFEL," J. Instrum. **16**, C12030 (2021).

Brodin, G. and Al-Naseri, H., "Anomalous conductivity due to relativistic Landau quantization," Phys. Rev. E **110**, 015204 (2024).

Bromage, J., Bahk, S.-W., Begishev, I. A., Dorrer, C., Guardalben, M. J., Hoffman, B. N., Oliver, J., Roides, R. G., Schiesser, E. M., and Shoup, M. J. III *et al.*, "Technology development for ultraintense all-OPCPA systems," High Power Laser Sci. Eng. **7**, e4 (2019).

Caiazzo, I., "QED and X-ray polarization from neutron stars and black holes," Ph.D. thesis (University of British Columbia, 2019).

Caiazzo, I., González-Caniulef, D., Heyl, J., and Fernández, R., "Probing magnetar emission mechanisms with X-ray spectropolarimetry," Mon. Not. R. Astron. Soc. **514**, 5024–5034 (2022).

Caiazzo, I. and Heyl, J., "Vacuum birefringence and the x-ray polarization from black-hole accretion disks," Phys. Rev. D **97**, 083001 (2018).

Caiazzo, I. and Heyl, J., "Polarization of accreting X-ray pulsars. I. A new model," Mon. Not. R. Astron. Soc. **501**, 109–128 (2020).

Courant, R., Friedrichs, K., and Lewy, H., "Über die partiellen Differenzengleichungen der mathematischen Physik," Math. Ann. **100**, 32–74 (1928).

Crouseilles, N., Hervieux, P.-A., Hong, X., and Manfredi, G., "Vlasov–Maxwell equations with spin effects," J. Plasma Phys. **89**, 905890215 (2023).

Crouseilles, N., Hervieux, P.-A., Li, Y., Manfredi, G., and Sun, Y., "Geometric particle-in-cell methods for the Vlasov-Maxwell equations with spin effects," J. Plasma Phys. **87**, 825870301 (2021).

Danson, C. N., Haefner, C., Bromage, J., Butcher, T., Chanteloup, J.-C. F., Chowdhury, E. A., Galvanauskas, A., Gizzi, L. A., Hein, J., Hillier, D. I. *et al.*, "Petawatt and exawatt class lasers worldwide," High Power Laser Sci. Eng. **7**, e54 (2019).

Esirkepov, T., "Exact charge conservation scheme for particle-in-cell simulation with an arbitrary form-factor," Comput. Phys. Commun. **135**, 144–153 (2001).

Ganse, U., Kilian, P., Siegel, S., and Spanier, F., "Numerical challenges in kinetic simulations of three-wave interactions," in *Numerical Modeling of Space Plasma Flows (ASTRONUM 2011)*, Astronomical Society of the Pacific Conference Series Vol. 459, edited by N. V. Pogorelov, J. A. Font, E. Audit, and G. P. Zank (Astronomical Society of the Pacific, 2012), p. 265.

Gil, J. and Mitra, D., "Vacuum gaps in pulsars and PSR J2144-3933," Astrophys. J. **550**, 383–391 (2001).

Gonoskov, A., Blackburn, T. G., Marklund, M., and Bulanov, S. S., "Charged particle motion and radiation in strong electromagnetic fields," Rev. Mod. Phys. **94**, 045001 (2022).

Gotthelf, E. V., Vasisht, G., Boylan-Kolchin, M., and Torii, K., "A 700 year-old pulsar in the Supernova Remnant Kesteven 75," Astrophys. J. **542**, L37–L40 (2000).

Greenwood, A. D., Cartwright, K. L., Luginsland, J. W., and Baca, E. A., "On the elimination of numerical Cerenkov radiation in PIC simulations," J. Comput. Phys. **201**, 665–684 (2004).

Grismayer, T., Torres, R., Carneiro, P., Cruz, F., Fonseca, R. A., and Silva, L. O., "Quantum electrodynamics vacuum polarization solver," New J. Phys. **23**, 095005 (2021).

Grismayer, T., Vranic, M., Martins, J. L., Fonseca, R. A., and Silva, L. O., "Laser absorption via quantum electrodynamics cascades in counter propagating laser pulses," Phys. Plasmas **23**, 056706 (2016).

Heisenberg, W. and Euler, H., "Consequences of Dirac theory of the positron," arXiv:0605038 (2006).

Kilian, P., Burkart, T., and Spanier, F., "The influence of the mass ratio on particle acceleration by the filamentation instability," in *High Performance Computing in Science and Engineering'11*, edited by W. E. Nagel, D. B. Kröner, and M. M. Resch (Springer Berlin Heidelberg, Berlin, Heidelberg, 2012), pp. 5–13.

Kim, C. M. and Kim, S. P., "Vacuum birefringence at one-loop in a supercritical magnetic field superposed with a weak electric field and application to pulsar magnetosphere," Eur. Phys. J. C **83**, 104 (2023).

Kim, D.-H., Kim, C. M., and Kim, S. P., "Quantum refraction effects in pulsar emission," Mon. Not. R. Astron. Soc. **531**, 2148–2161 (2024). https://academic.oup.com/mnras/article-pdf/531/1/2148/57953230/stae1304.pdf.

Kostenko, A. and Thompson, C., "QED phenomena in an ultrastrong magnetic field. I. Electron–photon scattering, pair creation, and annihilation," Astrophys. J. **869**, 44 (2018).

Kostenko, A. and Thompson, C., "QED phenomena in an ultrastrong magnetic field. II. Electron–positron scattering, e±–ion scattering, and relativistic Bremsstrahlung," Astrophys. J. **875**, 23 (2019).

Lindner, A., Ölmez, B., and Ruhl, H., "Numerical simulations of the nonlinear quantum vacuum in the Heisenberg-Euler weak-field expansion," J. Comput. Phys.: X **17**, 100124 (2023).

Lundin, J., "QED and collective effects in vacuum and plasmas," Ph.D. thesis (Umeå University, Department of Physics, 2010).

Manfredi, G., Hervieux, P.-A., and Hurst, J., "Phase-space modeling of solid-state plasmas," Rev. Mod. Plasma Phys. **3**, 13 (2019).

Medvedev, M. V., "Plasma modes in QED super-strong magnetic fields of magnetars and laser plasmas," Phys. Plasmas **30**, 092112 (2023).

Melrose, D. B., *Instabilities in Space and Laboratory Plasmas* (Cambridge University Press, 1986).

Mereghetti, S., Götz, D., Mirabel, I. F., and Hurley, K., "INTEGRAL discovery of persistent hard X-ray emission from the Soft Gamma-ray Repeater SGR 1806-20," Astron. Astrophys. **433**, L9–L12 (2005).

Pérez-García, M. A., Pérez Martínez, A., and Rodríguez Querts, E., "Remarks on propagating waves in non-linear vacuum electrodynamics," Eur. Phys. J. C **83**, 746 (2023).

Qu, K., Meuren, S., and Fisch, N. J., "Collective plasma effects of electron–positron pairs in beam-driven QED cascades," Phys. Plasmas **29**, 042117 (2022).

Rigoselli, M., Taverna, R., Mereghetti, S., Turolla, R., Israel, G. L., Zane, S., Marra, L., Muleri, F., Borghese, A., Coti Zelati, F., De Grandis, D., Imbrogno, M., Kelly, R. M. E., Esposito, P., and Rea, N., "IXPE detection of highly polarized x-rays from the magnetar 1E 1841-045," Astrophys. J. Lett. **985**, L34 (2025).

Rowlinson, A., Gompertz, B. P., Dainotti, M., O'Brien, P. T., Wijers, R. A. M. J., and van der Horst, A. J., "Constraining properties of GRB magnetar central engines using the observed plateau luminosity and duration correlation," Mon. Not. R. Astron. Soc. **443**, 1779–1787 (2014). arXiv:1407.1053 [astro-ph.HE].

Schoeffler, K. M., Grismayer, T., Uzdensky, D., Fonseca, R. A., and Silva, L. O., "Bright gamma-ray flares powered by magnetic reconnection in QED-strength magnetic fields," Astrophy. J. **870**, 49 (2019).

Schoeffler, K. M., Grismayer, T., Uzdensky, D., and Silva, L. O., "High-energy synchrotron flares powered by strongly radiative relativistic magnetic reconnection: 2D and 3D PIC simulations," Mon. Not. R. Astron. Soc. **523**, 3812–3839 (2023).

Schwinger, J., "On gauge invariance and vacuum polarization," Phys. Rev. **82**, 664–679 (1951).

Taverna, R. and Turolla, R., "X-ray polarization from magnetar sources," Galaxies **12**, 6 (2024).

Taverna, R., Turolla, R., Gonzalez Caniulef, D., Zane, S., Muleri, F., and Soffitta, P., "Polarization of neutron star surface emission: A systematic analysis," Mon. Not. R. Astron. Soc. **454**, 3254–3266 (2015).

Taverna, R., Turolla, R., Muleri, F., Heyl, J., Zane, S., Baldini, L., González-Caniulef, D., Bachetti, M., Rankin, J., Caiazzo, I., Lalla, N. D., Doroshenko, V., Errando, M., Gau, E., Kırmızıbayrak, D., Krawczynski, H., Negro, M., Ng, M., Omodei, N., Possenti, A., Tamagawa, T., Uchiyama, K., Weisskopf, M. C., Agudo, I., Antonelli, L. A., Baumgartner, W. H., Bellazzini, R., Bianchi, S., Bongiorno, S. D., Bonino, R., Brez, A., Bucciantini, N., Capitanio, F., Castellano, S., Cavazzuti, E., Ciprini, S., Costa, E., Rosa, A. D., Monte, E. D., Gesu, L. D., Marco, A. D., Donnarumma, I., Dovčiak, M., Ehlert, S. R., Enoto, T., Evangelista, Y., Fabiani, S., Ferrazzoli, R., Garcia, J. A., Gunji, S., Hayashida, K., Iwakiri, W., Jorstad, S. G., Karas, V., Kitaguchi, T., Kolodziejczak, J. J., Monaca, F. L., Latronico, L., Liodakis, I., Maldera, S., Manfreda, A., Marin, F., Marinucci, A., Marscher, A. P., Marshall, H. L., Matt, G., Mitsuishi, I., Mizuno, T., Ng, S. C.-Y., O'Dell, S. L., Oppedisano, C., Papitto, A., Pavlov, G. G., Peirson, A. L., Perri, M., Pesce-Rollins, M., Pilia, M., Poutanen, J., Puccetti, S., Ramsey, B. D., Ratheesh, A., Romani, R. W., Sgrò, C., Slane, P., Soffitta, P., Spandre, G., Tavecchio, F., Tawara, Y., Tennant, A. F., Thomas, N. E., Tombesi, F., Trois, A., Tsygankov, S. S., Vink, J., Wu, K., and Xie, F., "Polarized X-rays from a magnetar," Science **378**, 646–650 (2022).

Thompson, C. and Kostenko, A., "Pair plasma in super-QED magnetic fields and the hard X-ray/optical emission of magnetars," Astrophys. J. **904**, 184 (2020).

Vay, J.-L., Geddes, C. G. R., Cormier-Michel, E., and Grote, D., "Numerical methods for instability mitigation in the modeling of laser wakefield accelerators in a Lorentz-boosted frame," J. Comput. Phys. **230**, 5908–5929 (2011).

Yee, K. S., "Numerical solution of initial boundary value problems involving Maxwell's equations in isotropic media," IEEE Trans. Antennas Propag. **14**, 302–307 (1966).

Younes, G., Baring, M. G., Harding, A. K., Enoto, T., Wadiasingh, Z., Pearlman, A. B., Ho, W. C. G., Guillot, S., Arzoumanian, Z., Borghese, A., Gendreau, K., Göğüş, E., Güver, T., Van Der Horst, A. J., Hu, C.-P., Jaisawal, G. K., Kouveliotou, C., Lin, L., and Majid, W. A., "Magnetar spin-down glitch clearing the way for FRB-like bursts and a pulsed radio episode," Nat. Astron. **7**, 339–350 (2023).

Zhang, P., Bulanov, S. S., Seipt, D., Arefiev, A. V., and Thomas, A. G. R., "Relativistic plasma physics in supercritical fields," Phys. Plasmas **27**, 050601 (2020).

Zhang, Z., Aboushelbaya, R., Ouatu, I., Denis, E., James, A., Timmis, R. J. L., Von Der Leyen, M. W., Norreys, P. A., Torres, R., Grismayer, T., and Silva, L. O., "Computational modelling of the semi-classical quantum vacuum in 3D," Commun. Phys. **8**, 224 (2025).